Accepted Manuscript

A modelling technique for calculating stress intensity factors for structures reinforced by bonded straps. Part II: Validation

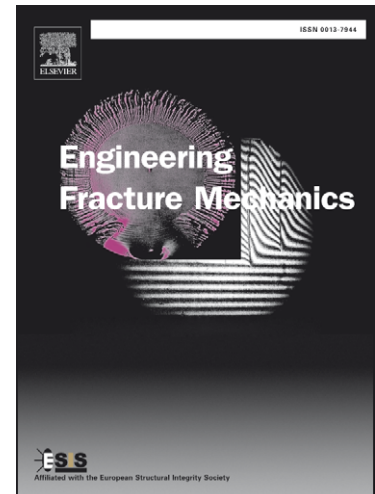M. Boscolo, X. Zhang

A modelling technique for calculating stress intensity factors for structures reinforced by bonded straps.

Part II: Validation

M. Boscolo [a,1], X. Zhang [a,*]

[a]*Department of Aerospace Engineering, Cranfield University, Bedfordshire, MK43 0AL, UK*

Abstract

In this second part of the two-part paper validation of the 2D FE modelling technique described in the first part is presented for a range of test configurations. Each mechanism that influences crack growth behaviour of strap reinforced structures is modelled for different substrate geometries, strap materials and dimensions in order to test the accuracy and robustness of the methodology. First, calculated through-thickness strain energy release rate distribution is compared with the result of a 3D FE model to validate this 2D model. Second, calculated disbond areas, thermal residual stresses and their redistribution with crack propagation are validated against experimental measurements. Third, influence of geometric nonlinearity and the need to use the alternate analysis method described in Part I are demonstrated by examples, and errors generated by not following this analysis rule are given. Finally, using the 2D model calculated stress intensity factors, fatigue crack growth rates and lives are predicted for different specimens, strap materials and applied stress levels and are compared with the experimental tests. Good or acceptable agreement has been achieved for each case.

Key words: bonded crack retarders, selective reinforcement, fatigue crack growth life, thermal residual stresses, delamination, secondary bending, composite patch repairs

* Corresponding author. Tel.: +44 1234 754621

Email address: `xiang.zhang@cranfield.ac.uk` (X. Zhang).

[1] Present address: School of Engineering and Mathematical Sciences, City University London, Northampton square, EC1V

1. Introduction

Integral structures can be designed and fabricated to be lighter and cheaper than the conventional mechanically fastened assemblies, but they generally lack redundant structural members. Consequently, cracks will propagate much faster once initiated and without the means of crack retarders or stoppers. In order to satisfy the regulator's requirements and make the integral structures fail safe, crack retarders must be used [1–5]. Physical testing of all designs and strap choices is virtually impossible; hence a reliable analysis tool is needed.

In the first part of this two-part paper, a comprehensive 2D FE model is presented for calculating crack tip stress intensity factors (SIF) and then predicting fatigue crack growth (FCG) life of structures reinforced by bonded straps [6]. Some modelling techniques are available in the literature to study this problem [7–15], but a model including all the known effects which influence the life has never been attempted before. Lena et al. [11] have developed a methodology which deals with most of the effects. They studied double sided reinforced plates by using the modelling technique developed by Sun et al. [7–10]. Due to the symmetric configuration no secondary bending was generated, then no effect of bending on the SIF needed to be considered and, moreover, the crack profile through the thickness is symmetric which simplifies the analysis. Double sided reinforcements are not only simpler to model, but they are also more effective in retarding crack propagation. However, they cannot be used to comply with other design needs such as maintaining the external shape of fuselage and wings for aerodynamic reasons. Lena et al. [11] included also the effect of thermal residual stresses (TRS) in their analysis. The curing temperature of the adhesive was not assumed as described in [6] but was assessed by running different models at different trial temperatures to compute the FCG lives and, by comparing the predicted FCG lives with the experimental one, the curing temperature of the adhesive was found. Clearly, using this procedure, any possible error encountered in computing the SIF and the scatter showed by the test will be absorbed in the curing temperature which was found to be of just 42 °C when it should have been of 100 °C as showed in [6] and confirmed by experiments in section 3.3. Moreover, due to the lack of experimental data, the effect of the TRS was considered to increase the maximum SIF instead of changing the R-ratio as it was explained in [6].

In contrast with previous methodologies, the modelling technique presented in part I [6] was developed to take account of all main mechanisms involved in bonded strap reinforced structures, such as the beneficial actions of stiffening and crack bridging, the adverse effects of thermal residual stresses and adhesive disbond,

0HB

2

as well as the secondary bending and non-uniform crack profile through the thickness. The aim of this second part of the paper is to present the modelling results against experimental tests found in the literature [3–5] for validation purpose. Firstly, the method to compute the non-uniform distribution of SIF through the thickness by using 2D FE analysis is validated against 3D FE results (section 3.1). Secondly, calculated disbond shape and area are compared with experimental measurements found in [3] (section 3.2). Thirdly, TRS are calculated by running a thermal load analysis to simulate the consequence of adhesive curing process and for keeping the residual stress field in the analysis models before applying external stresses in order to simulate the redistribution behaviour of these stresses during substrate crack propagation. Calculated values are compared with experimental measurements in [16,17] in section 3.3 for different strap materials and geometries. The coupling effect between the thermal and mechanical loads is analysed in section 3.4, which also shows the errors caused by the usually used superposition method. Finally predicted FCG lives of three different reinforced plates are compared with experimental results in [3,4] to validate the modelling methodology (section 3.5).

2. Experimental validation data

To validate the modelling technique described in [6], test results reported in an experimental investigation conducted by Irving and Figueroa-Gordon et al [3–5] have been used. In this work single edge notch tension (SENT) and middle crack tension M(T) samples of $7085-T7651$ aluminium alloy , 10 mm thick, were subjected to fatigue loading. The material fatigue crack growth rates for $7085-T7651$ is shown in figure 1 where the curves for R ratio of 0.1 and 0.6 were obtained by fitting the test data in [18], and curves for other R ratios are obtained by using the Harter T-method [19]. Test samples with bonded straps are shown in figure 2. Straps in [3–5] were made of four different materials, which were the glass fibre reinforced polymer (GFRP), carbon fibre reinforced polymer (CFRP), titanium alloy Ti-6AL-4V (Ti-6-4), and the fibre-metal laminate called GLARE I 3/2 (GLARE). These straps were bonded to the substrate using FM 94 adhesive cured at $120°C$. Mechanical properties of the strap and substrate materials, used as input to the predictive model described in [6], are given in table 1. Strap dimensions were variable. A notation is used in this work to specify the strap dimensions, which is $wXXdYYtZZlSSS$, where w is the strap width, d the distance between strap edge and initial crack tip, t the strap thickness, and l the strap total length. For example, $w20d2.5t4.4l180$ defines a strap of 20 mm wide, 2.5 mm from the initial crack tip, 4.4 mm thick, and 180 mm long.
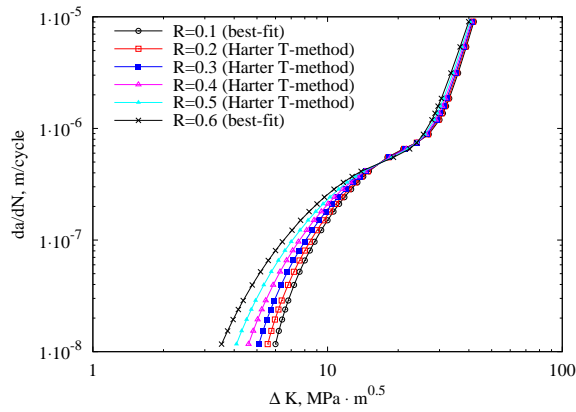
3

Fig. 1. Material fatigue crack growth rate for aluminium alloy 7085-T7651. Curves for $R = 0.1$ and 0.6 are best-fitted lines of the test data from [18] and the others are obtained by using the Harter T-method [19].
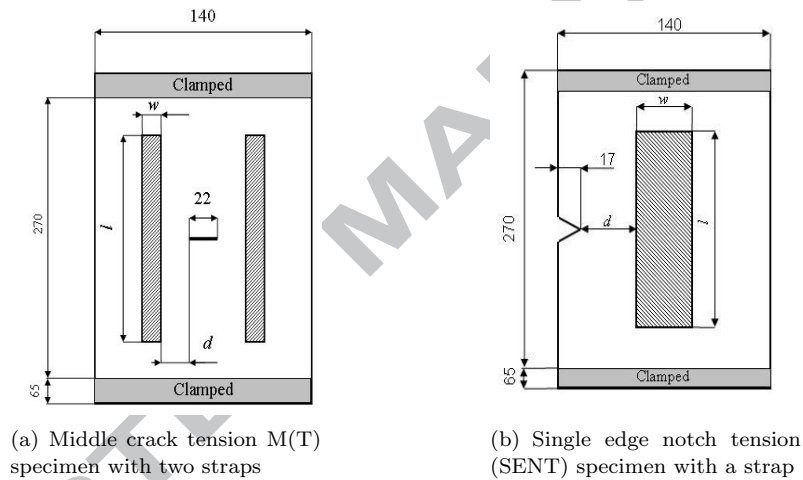

(a) Middle crack tension M(T) specimen with two straps

(b) Single edge notch tension (SENT) specimen with a strap

Fig. 2. Geometry and dimension of two test specimens. Strap dimensions are variable. Sketches not to scale.

3. Modelling technique validation

3.1. *Stress intensity factor through-thickness distribution*

The first step of methodology validation was to compare the through-thickness distribution of the strain energy release rate (SERR) and stress intensity factor (SIF) obtained by the 2D model with those by a 3D FE model.

The SENT sample (figure 2(b)) was used for this purpose with an initial crack length of 32 mm reinforced by a titanium strap of dimension $w20d5t2l200$. The analysis was conducted at $\sigma_{max} = 18.57$ MPa. The specimen was found to be in the plane stress condition, thus the appropriate equation presented in [6] was used to obtain SIF from calculated SERR. Neither the thermal residual stress nor adhesive disbond was

4

Table 1
Mechanical properties of substrate, strap and adhesive materials.

Material	Aluminium[*]	Adhesive [†]	carbon-epoxy	glass-epoxy	Titanium[ℵ]	GLARE I 3/2[§]	
						Aluminium	glass epoxy
Type	7085-T7651	FM 94	Cycom 919HF-42%-HS	Hexcel 913	Ti-6Al-4V	7475-T761	S2
E_1 (GPa)	71.0	1.90	135.0[‡]	46.0[‡]	113.8	70.3	48.9
E_2 (GPa)	71.0	1.90	9.65[♮]	8.6 [♮]	113.8	70.3	5.5
G_{12} (GPa)	26.7	0.62	4.55[♮]	3.8[♯]	42.4	26.43	5.5
ν_{12}	0.33	0.52	0.3[♮]	0.28[♯]	0.342	0.330	0.330
α_{11} ($\mu°C^{-1}$)	23.6	/	-0.3[*]	7[*]	8.6	23.2	6.10
α_{22} ($\mu°C^{-1}$)	23.6	/	30[*]	21[*]	8.6	23.2	2.62
ρ (g/cm^3)	2.77	1.1	1.8[*]	2[*]	4.51	2.81	1.95

[*] Generic properties.

[†] In the absence of published mechanical properties for this adhesive, the properties of Hexcel Redux 810 are used as typical values. Data sheet www.hexcel.com, access date Dec 2006.

[‡] Values from [20].

[♮] Generic CFRP www.composite.about.com/library/data/blc-t300-934-1.htm, access date April 2008.

[♯] Generic GFRP www.composite.about.com/od/data/l/blg_egepoxy.htm, access date April 2008.

[ℵ] Titanium alloy grade 5 www.asm.matweb.com/search/SpecificMaterial.asp?bassnum=MTP641, access date April 2008.

[§] Courteously from Erik J. Kroon, GTM-advanced structures.

considered in this analysis in order to focus on validating the method of using 2D plate finite elements with multi-point constraint (MPC) to take account of the secondary bending effect. SERR and SIF were calculated for each crack length.

Firstly, calculated SERR through-thickness distributions are shown in figure 3 for two crack lengths. The so-called top surface is where the strap is bonded ($z = 10$ mm). SERR obtained by the 2D model (noted as $G_I\,2D$) is in good agreement with that obtained by 3D model ($G_I\,3D$). A parabolic fitting curve is also plotted ($G_I\,3D$ par) to show it fits perfectly with the result by the 3D model with exception at the top and bottom surfaces of the plate. This confirms that the SERR distribution has a parabolic shape. The discrepancy at the top and bottom faces may be explained by the crack tip stress singularity; when crack intersects with a free surface, the order of stress singularity differs from the inverse-square-root singularity of a 2D (through-thickness) crack problem described by the Westergaard stress function, thus, at the plate surface a crack cannot be characterised by the SIF [21].

The corresponding SIF through-thickness distribution are shown in figure 4. Again 2D ($K_I\,2D$) and 3D ($K_I\,3D$) results are in good agreement. The 2D SIF looks like a straight line, but it is actually the square root of a parabola, which is reduced closely to a line. A fitting line ($K_I\,3D$ lin) is plotted to extrapolate the

3D SIF values to the top and bottom faces of the plate; it does not fit the results as well as the parabolic fit does for the SERR. This is because that SIF is not strictly a straight line.

In figure 5 the SERR and SIF at the top (reinforced side) and bottom faces are plotted against crack length (a) and compared with the mean SERR and its corresponding SIF (root mean square value) obtained by the 2D and 3D analyses. Good agreement is archived between 2D and 3D models for each crack length. Therefore the 2D model is validated in terms of the SERR and SIF through-thickness distributions by taking into account of the secondary bending effect.
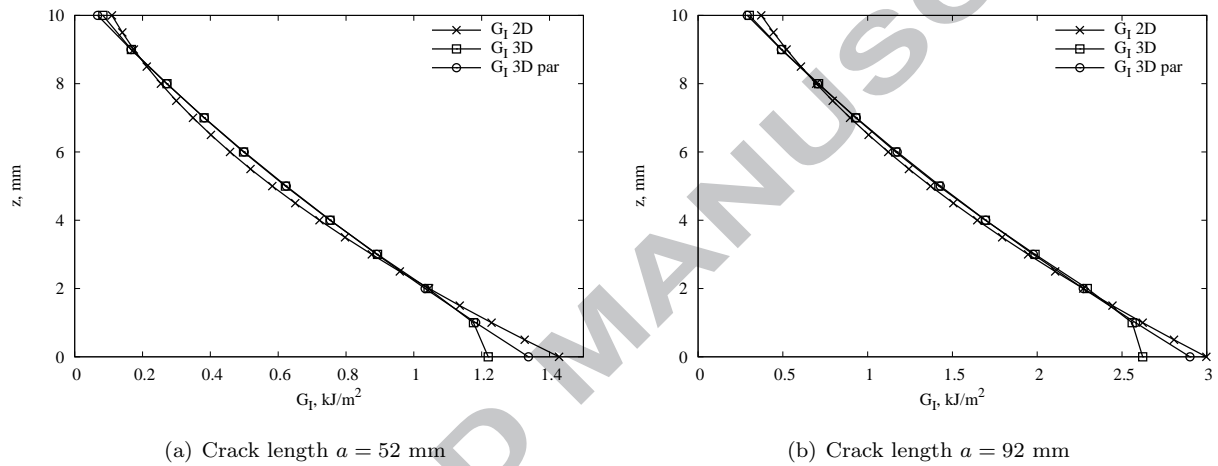

(a) Crack length $a = 52$ mm

(b) Crack length $a = 92$ mm

Fig. 3. SERR through-thickness distribution: SENT sample with titanium strap $w20d5t2l200$.
($z = 10$ mm is on the strap side)

(a) Crack length $a = 52$ mm
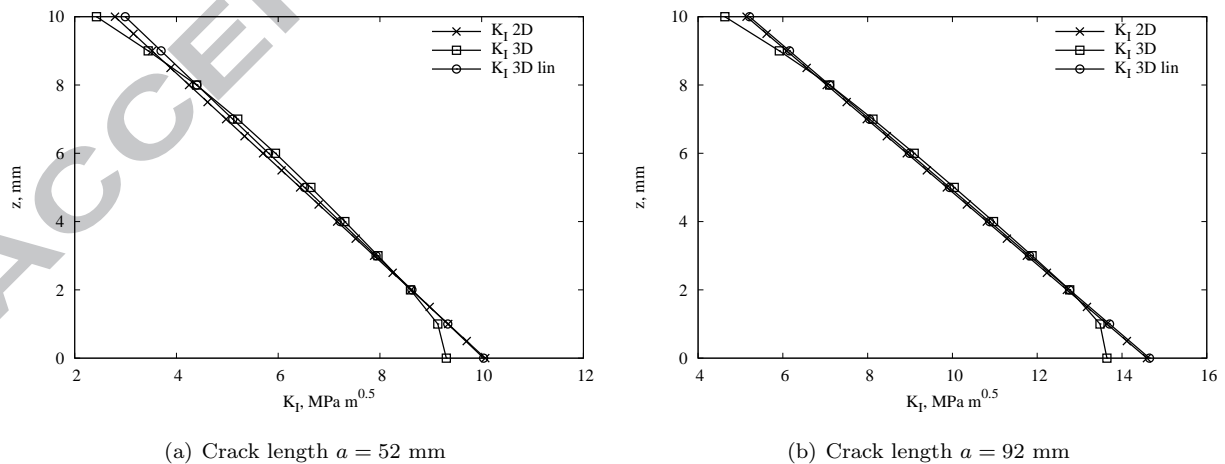
(b) Crack length $a = 92$ mm

Fig. 4. SIF through-thickness distribution: SENT sample with titanium strap $w20d5t2l200$.
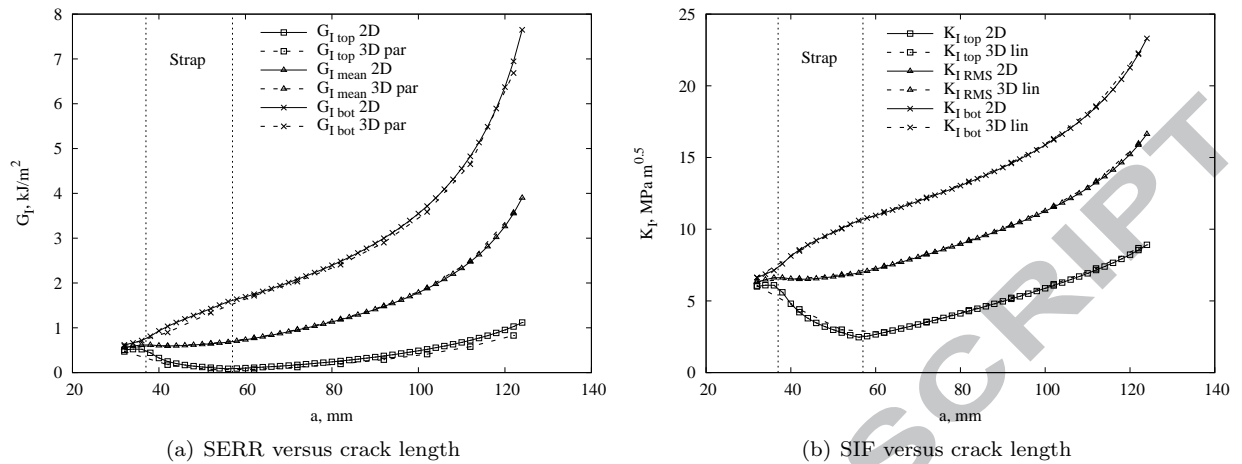
6

Fig. 5. Comparison of 2D (solid lines) and 3D (dashed lines) model calculated SERR and SIF values in different thickness positions (top "□", bottom "×", mean and RMS "△"). SENT sample with titanium strap $w20d20t2l200$.

3.2. *Progressive disbond failure*

Another important mechanism in bonded crack retarder problem is the progressive disbond of adhesive that reduces the effectiveness of the strap. This progressive disbond should be adequately modelled in order to achieve good prediction of FCG life. Both the SENT and M(T) specimens were used in this analysis . The SENT had an initial crack length (a_o) of 32 mm and was reinforced by a titanium strap of $w20d5t2l200$. Applied cyclic stress was $\sigma_{max} = 18.57$ MPa, $R = 0.1$. The M(T) had an initial crack length ($2a_o$) of 22 mm and was reinforced by a GFRP strap of dimensions $w20d2.5t4.4l180$. Applied cyclic stress was $\sigma_{max} = 60$ MPa, $R = 0.1$.

Predicted final disbond shape and area are compared with the experimental measurements in [3,4]. Before discussing the comparisons, the meaning of final disbond damage needs some clarification. In the experimental test, disbond grew progressively and two failure modes were observed when substrate crack reached its critical length, i.e. either one side of the strap (divided by the crack growth path) debonded completely from the substrate and the experiment stopped, or the two "parts" of the substrate (separated by the crack) were kept connected, or bridged, by the strap and the test machine kept running even the substrate had broken into two pieces. In the second case, although the structure could still stand the load, the test was considered finished since the substrate had failed. During the experiment it was often difficult to decide if the strap had debonded completely and, subsequently, the sample failed, or the substrate had failed before the strap debonded completely on one side of the crack because the adhesive was unable to transfer all the load to the strap. Conventionally the final disbond area is defined as the adhesive failure area obtained at

7

the end of the test, i.e. when the reinforced plate fails due to either of the two modes. If one side of the strap is completely debonded, then the area on the other side is taken as final disbond damage extent. From the modelling point of view, final disbond area is obtained by one of the following definitions: 1) when strap debonds from substrate completely; 2) the disbond area at the critical crack length in the substrate.

Figure 6(a) shows the comparison of calculated and measured final disbond shape for the titanium strap reinforced SENT sample. In the figures only the lower half of the strap is shown and the disbond and bonded areas are indicated. Substrate crack growth path was from the upper left corner to the right as indicated. Predicted and measured final disbond shape and area are in good agreement.

Disbonds in the M(T) plate reinforced by two GFRP straps are shown in figure 6(b). The agreement between the predicted and measured [3,4] disbond areas are not as good as for the SENT sample with titanium strap. The actual disbond damage has two disbond fronts: one was close to the substrate crack (upper part in the figure) and the other started from the bottom corner of the strap (strap end edge). The modelling work did not find this second disbond front because disbond initiation is primarily driven by the passing of substrate crack. However, by analysing the FE calculated stresses in the adhesive it is found that, for an un-cracked substrate, the maximum shear stress is actually developed at the strap free ends (bottom corners in figure 6(b)) as well as the maximum peal stress which is constant on the bottom free edge of the strap. The mixed mode caused by the peel and shear stress is likely to cause this second disbond front on the free edges of the straps, starting from the corners and growing towards the middle of the strap under joint action of shear and peel.

3.3. *Thermal residual stresses and their redistribution with crack growth*

Thermal residual stresses (TRS) are caused by curing adhesive at elevated temperature. They influence FCG rate and should be considered in predictive models. TRS can be experimentally measured, but testing is time and money consuming. For this reason a modelling technique has been developed.

In this paper residual stresses in the SENT sample reinforced by straps of different dimensions and materials are presented to demonstrate the robustness of the methodology presented in [6]. Adhesive FM94 was cured at 120 °C. There are two steps in the analysis: the first is to determine the initial residual stress distribution after the curing process; the second is to model a series of stress re-distribution during crack propagation. Calculated residual stresses are plotted along the sample's width in three different thickness positions (figure 7).

(a) SENT sample and Ti strap
$w20d5t2l200$.

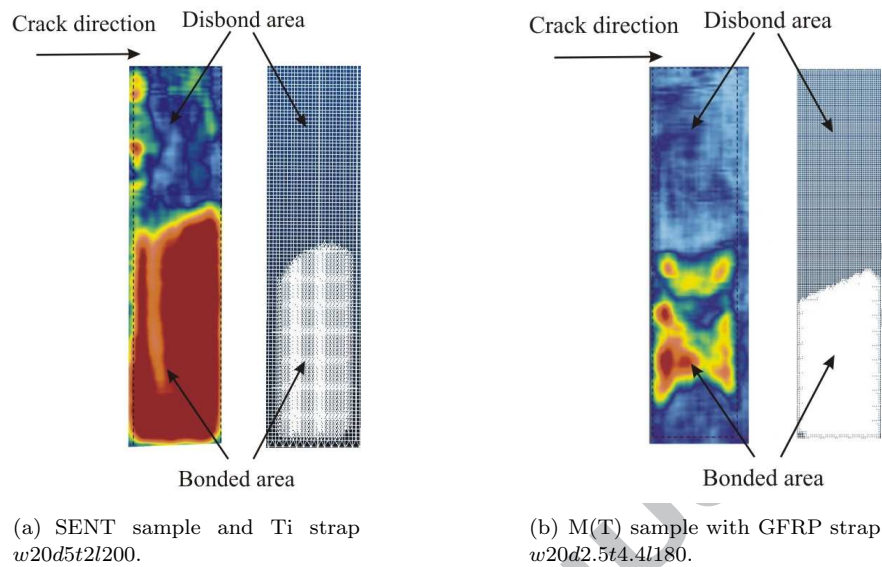(b) M(T) sample with GFRP strap
$w20d2.5t4.4l180$.

Fig. 6. Final disbond shapes: modelling (right) vs. experimental measurements (left) [3,4]. Only half of the strap is illustrated. Dimensions in figure 2
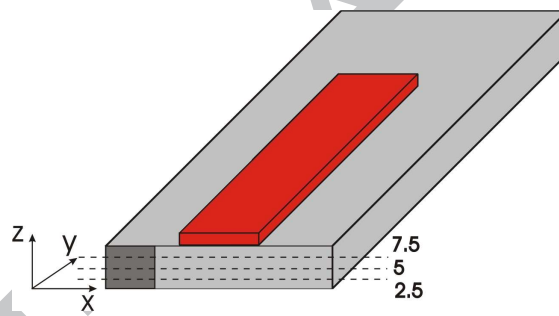

Fig. 7. SENT specimen and different thickness position lines along which TRS were calculated and measured.

Predictions obtained by the 2D FE modelling technique presented in the first part of the paper [6] are compared with the experimental measurements obtained by Liljedahl et al. as part of the same project and reported in [16,17]. The measurements of residual stress profiles in the substrate were obtained by using the neutron diffraction technique, which is a well-established non-destructive method that can measure through-thickness residual stress distributions. Experimentally measured TRS are reported in [16] for samples reinforced by titanium straps and in [17] for all other strap materials. Calculated initial TRS distribution is plotted against experiments in figure 8 for different strap materials, widths and thicknesses. For each strap configuration, the calculated and measured are in reasonably good agreement. Discussions for each strap configuration are given below.

Figures 8(a) and 8(b) show the initial stress distribution for the titanium strap cases. Two different strap thickness ($w20d20t2l200$ and $w20d20t4l200$) were used. Although the cure temperature, the elastic modulus

9

and coefficient of thermal expansion (CTE) are all the same for the two cases, TRS produced by the thicker (4 mm) strap are higher. This is because that thicker strap is stiffer, consequently when the temperature drops to the room temperature the strap does not contract with the substrate as much as the thinner strap will do and the displacements compatibility between strap and substrate is achieved at a higher stress level in the substrate. It is also worth noting the stress concentration spot beneath the strap, i.e. the "bump" feature in the graphs related to the Ti strap; the reason will be discussed in the next paragraphs.

Strap width effect can be seen by comparing figure 8(a) with 8(d) ($w20d20t2l200$ vs. $w100d20t2l200$) and 8(b) with 8(c) ($w20d20t4l200$ vs. $w60d20t4l200$) where TRS caused by titanium straps of different widths are plotted. Peak stress values for the wider straps are higher due to the higher stiffness. Therefore, the stiffer the strap, the higher the TRS peak values.

Stresses caused by straps of the same dimensions ($w20d20t2l200$) but different materials are plotted in figures 8(a), 8(e), and 8(f), respectively for the titanium, GFRP, and CFRP straps. TRS are strongly influenced by material's CTE and elastic modulus. Observation from these results is: the stiffer the strap and the lower the longitudinal CTE, the higher the TRS. The CFRP strap produces the highest TRS (figure 8(f)), followed by the titanium strap (figure 8(a)) and then the GFRP (figure 8(e)); GFRP has the lowest longitudinal elastic modulus.

Neither the CFRP nor the GFRP straps produced the distinct "bump" feature beneath the strap as the titanium strap does 8(a). The "bump" is caused by the titanium alloy's isotropic property; hence the strap does not contract in the transverse direction (x-direction) at the same rate as the aluminium substrate during the temperature drop, since the CTE of the titanium (8.6 $\mu°C^{-1}$) is much lower than that of the aluminium (23.6 $\mu°C^{-1}$). This causes tensile residual stress also in the x-direction that due to the Poisson's effect will make the substrate contract in the y-direction adding extra residual stress to what caused by the y-direction contraction. However, since the substrate and strap have to satisfy the displacement compatibility requirement, there is an increase in σ_{yy} beneath the strap. No "bump" for GFRP and CFRP reinforced cases because the CTE in the transverse direction (α_{22}) of this two polymer composites (respectively 30 and 21 $\mu°C^{-1}$) is very close to that of the aluminium substrate (23.6 $\mu°C^{-1}$); consequently, in the transverse or the x-direction, these straps contract at the same rate of the aluminium substrate during the temperature drop causing no further increase in the y-direction stresses.

When the crack propagates, TRS will re-distribute, that will in turn influence the crack growth rate. The SENT sample reinforced by titanium strap ($w20d20t2l200$) is used to demonstrate the analysis for four different crack lengths. Figure 9 shows the predicted TRS at two thickness positions (see figure 7) and
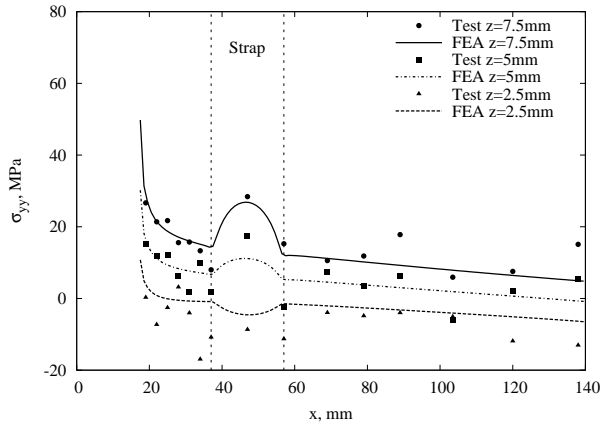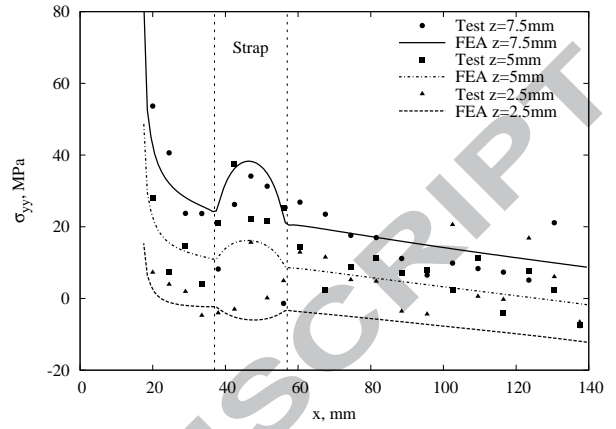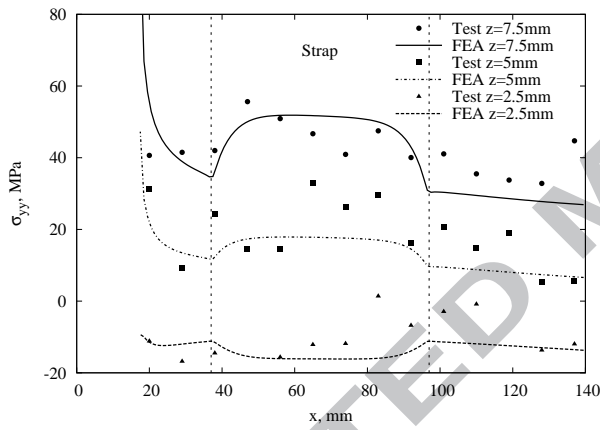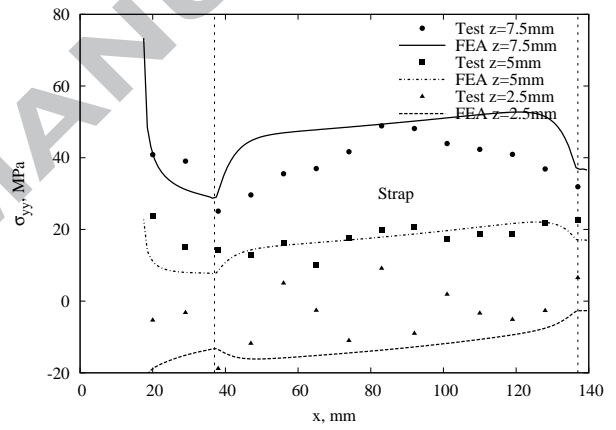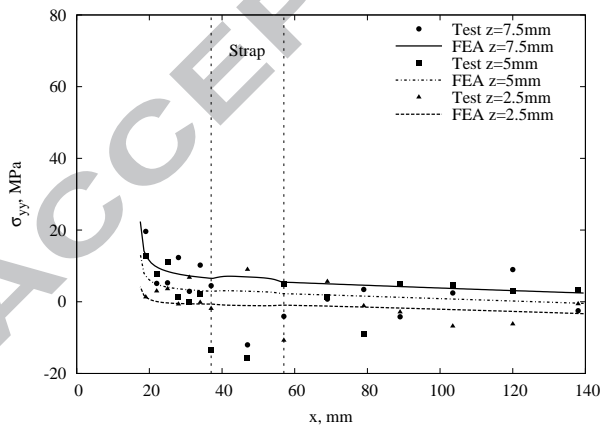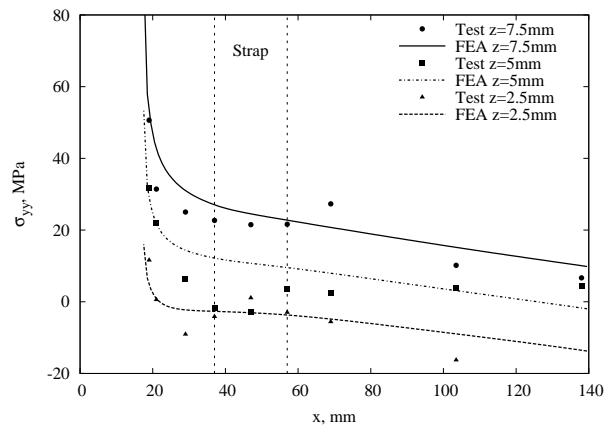
Fig. 8. Initial distributions of residual stresses in the longitudinal direction in the SENT bonded with various straps: computation (2D FEA) vs. measurement [16,17].

11

comparison with the experimental measurements in [22]. Good agreement is achieved for each crack length. Figure 9(a) shows the TRS distribution for crack length $a = 29$ mm, i.e. just before the crack tip entered the strap. The peak stress value is not really meaningful due to the dependence on the model mesh size. Figure 9(b) shows the TRS when crack is beneath the strap ($a = 47$ mm) and figures 9(c) and 9(d) show the stresses when crack has just passed the strap ($a = 69$ mm) and far from the strap ($a = 90$ mm).

From these analysis, it can be concluded that the distribution and magnitude of the TRS due to the curing process and their subsequent redistribution during crack propagation can be determined by the modelling method presented in [6].
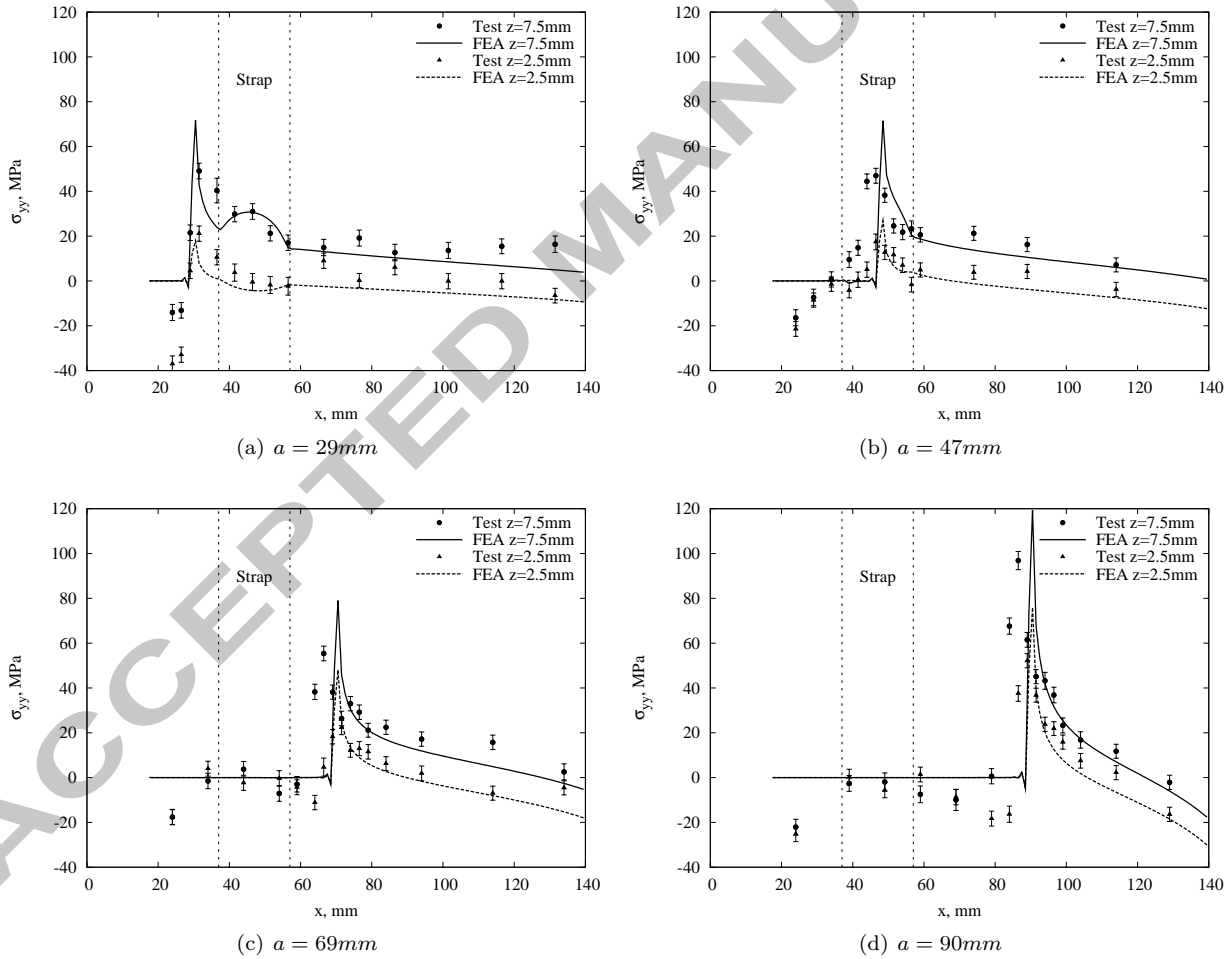

Fig. 9. Redistribution of TRS with crack propagation: computation (2D FEA) vs. measurement for SENT sample with titanium strap $w20d20t2l200$. Experiments from [22].

12

3.4. *Influence of geometric nonlinearity and thermo-mechanical coupling*

It is mentioned in the first part of this paper [6] that a dimensionless stress intensity factor (β) that is only a function of the geometry does not exist for this bonded structure due to the geometric nonlinearity. It will be demonstrated in this section that change in the applied load magnitude or the presence of TRS will change the value of β. There are two reasons for this. First, the magnitude of secondary bending is a function of the applied load; second, the extent of disbond damage also depends on the applied load and a different disbond area means a different geometry factor β.

In this study, the root mean square (RMS) value of the through-thickness SIF range, ΔK, is determined by the alternate analysis method [6] and is used for predicting FCG life. The β factor is defined by:

$$\beta = \frac{\Delta K}{\Delta \sigma \sqrt{\pi a}} \tag{1}$$

where, $\Delta \sigma$ is the applied stress range and a the crack length.

In figure 10(a) β factor versus crack length is plotted for two SENT plates reinforced by titanium strap of dimension $w20d20t2l200$. One sample was cured at the room temperature and the other at $120\,^\circ$C. Therefore, just the effect of the TRS can be seen in the β solution. Initial crack length was $a_o = 17$ mm and applied stress was $\sigma_{max} = 18.57$ MPa and $R = 0.1$, referred to as the "low load" case in this work. The curves can be split into two parts according to the crack length. When $a \leq 50$ mm, β value is lower for the sample cured at elevated temperature (low load + TRS), because the TRS try to bend the plate in the opposite direction to that of the secondary bending due to the applied load; this reduces the overall bending and consequently the β factor. When $a \geq 50$ mm, the difference in β solution is caused by the different disbond area. When there are TRS, adhesive is more stressed and the disbond damage is larger and β is higher. It is known in the literature that TRS do not influence the β solution because the effect of TRS should be equal at the maximum and minimum applied stresses and consequently should not affect the SIF range, only the effective R ratio is changed [23,24]. This is true when there is no secondary bending involved, e.g. welded joints or cold worked samples. However, in this case, TRS affect the bending direction and magnitude, and consequently they will influence the SIF range. Therefore, conventional β solution by normalisation does not exist.

Another comparison is shown in figure 10(b) where the SENT plate is subjected to the "high load" ($\sigma_{max} = 60$ MPa) and "low load" ($\sigma_{max} = 18.57$ MPa). Therefore the effect of the applied load on β solution can be seen. Again the curves can be split into two regions separated by crack length $a = 40$ mm. In the first

13

region only the effect of the load on the secondary bending can be seen because the adhesive has not yet started debonding. Higher load causes more bending, thus higher β factor. In the second region ($a > 40$ mm) adhesive is failing and higher load cause more adhesive disbond and consequently higher β values.

Another important factor mentioned in [6] is that the mechanical and thermal loads must be applied at the

(a) Dependency of β on thermal residual stress

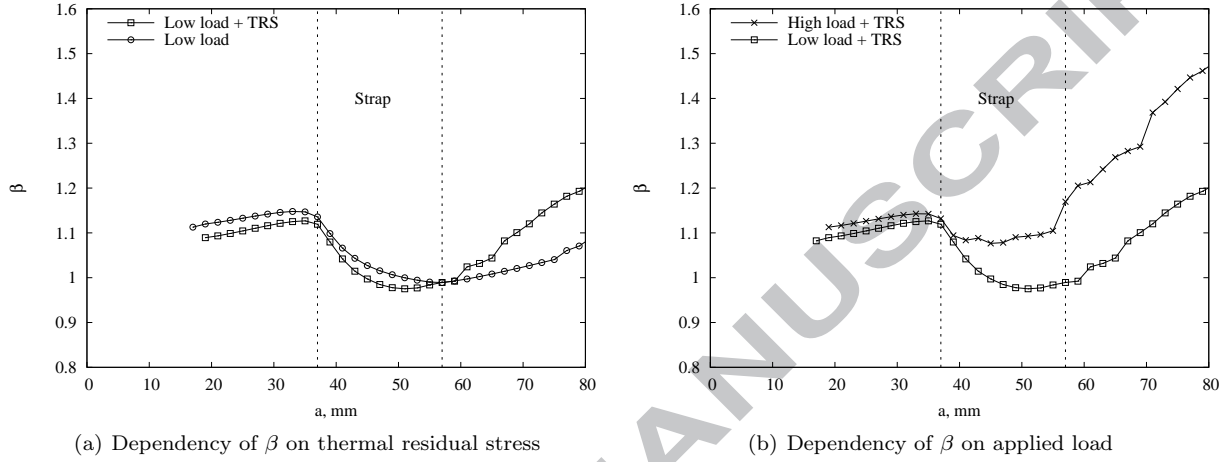(b) Dependency of β on applied load

Fig. 10. Influence of geometric nonlinearity on the dimensionless SIF (β) due to different magnitude of secondary bending and disbond. SENT sample with titanium strap $w20d20t2l200$.

same time and the stress intensity factor is computed by a single FE analysis. This is due to the interaction between the mechanical and thermal loads; consequently, superposition of two separate analysis results may lead to erroneous solution. In fact, each load causes bending in opposite directions; hence the overall deformed shape affects the SIF and should be determined by considering both stress fields in one single analysis. To demonstrate this effect the SENT sample with the titanium strap is modelled at the low stress (18.57 MPa). Calculated SIF values due to the mechanically applied stress (indicated by K_{app}), thermal residual stress (K_{res}), simple summation of the separate solutions ($K_{app} + K_{res}$), and the total SIF obtained by a joint thermo-mechanical analysis (K_{tot}) are plotted against crack length (a) in figure 11(a). It can be seen that the coupling effect of the thermal and mechanical loads is not negligible. The errors (Err) caused by neglecting the coupling effect can be estimated as:

$$Err = \frac{K_{tot} - (K_{app} + K_{res})}{(K_{app} + K_{res})} \times 100 \tag{2}$$

Errors are also illustrated in figure 11(a) referring to the right axis. It is between -12% and $+20\%$. The same analysis was performed for the higher applied stress (60 MPa) and the results are shown in figure 11(b). The error by superposition is slightly smaller (between -4% and $+8\%$), but still not negligible. This is because that higher applied load means higher applied SIF, then the contribution of residual SIF to the

14

total SIF is relatively smaller, thus smaller error.

This analysis has demonstrated that due to the influence of secondary bending and adhesive disbond, the β solution is also function of the applied load. Thus the SIF range must be computed case by case and a geometry factor β solution does not exist. Moreover, the coupling effect of thermal and mechanical loads on secondary bending requires both load fields being taken into account in one FE analysis to compute the SIF; if the superposition method is applied, one might encounter an error of 20%.
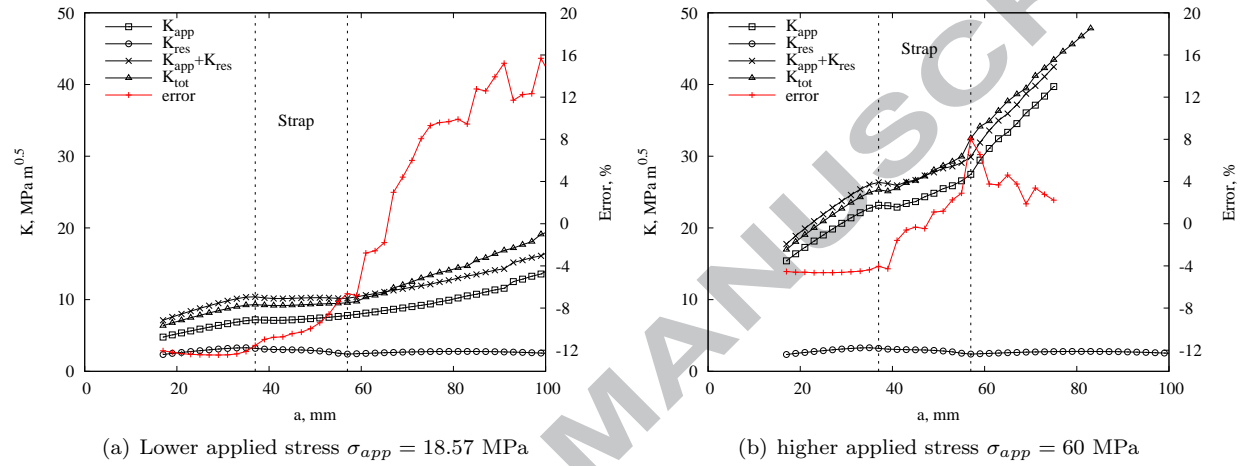

(a) Lower applied stress $\sigma_{app} = 18.57$ MPa

(b) higher applied stress $\sigma_{app} = 60$ MPa

Fig. 11. Interaction of mechanical and thermal residual stresses at low and high applied loads. SENT sample with titanium strap $w20d20t2l200$.

3.5. *FCG life prediction*

Each previously examined mechanism influences the crack growth driving force SIF, and hence the accuracy in fatigue crack growth life prediction. Therefore, the ultimate validation test is to compare predicted FCG rate and life with test results. Following example samples were reinforced by straps made of the titanium, GLARE, and GFRP; mechanical properties used in the predictive models are given in table 1.

The first validation analysis was for the SENT plate reinforced by a titanium strap of dimension $w20d5t2l200$. The initial crack length a_o was 32 mm and the applied stress was $\sigma_{max} = 18.57$ MPa, $R = 0.1$. Predicted FCG rate and life are compared with the test results found in [3] in figures 12(a) and 12(b). Both root mean square (RMS) and weighted (w) value of the SIF range were used for the prediction. Good agreement is achieved by the weighted solution in terms of the FCG rate before the crack tip has passed the strap. After that point calculated crack growth rate using the weighted SIF was slightly faster giving a conservative prediction of FCG life (error -17.1%). The RMS SIF produced a slightly lower crack growth rate at the

15

beginning and faster at the end giving a final value of number of cycle really close to the measured one (error $+0.42\%$).

The second validation case used the M(T) plate reinforced by GLARE straps of dimension $w10d8t5.4l180$. The initial half crack length a_o was 20 mm and the applied stress was $\sigma_{max} = 26.38$ MPa, $R = 0.1$. The experimental results are taken from [18]. Predicted FCG rate and life are showed in figures 12(c) and 12(d), respectively. Again both weighted and RMS SIF values are used for the prediction. Using the weighted SIF solution calculated FCG rate is in excellent agreement with the test results for crack lengths $a > 30$mm. However, since at the beginning the calculated FCG rate is slightly higher than the experimental measured, the predicted life is conservative (error -13.5%). The RMS solution is in good agreement up to a crack length of 30 mm but after that, it underestimates the FCG rate resulting error of $+9.3\%$ in the final life.

The last case is the M(T) plate reinforced by GFRP straps of dimension $w20d2.5t4.4l180$. The initial half crack length a_o was 11 mm and applied stress was $\sigma_{max} = 60$ MPa, $R = 0.1$. The experimental results can be found in [4]. The results are shown in figures 12(e) and 12(f). The weighted solution is in good agreement with the test until the crack approached the end of the strap and, after that, the crack growth rate is slightly overestimated causing an error of -15.5% in the final FCG life. The RMS solution produces a lower crack growth rate at the beginning and higher at the end resulting in a prediction error of 0.5%.

A summary of the prediction and respective errors is given in table 2. Using the weighed SIF values produces FCG lives that are consistently conservative. The lowest error values are obtained by the RMS SIF with error range lower than 10%, but sometimes it overestimated the life. It seems that when a conservative solution is needed the weighed SIF value should be used for life prediction. If an idea of the FCG life is wanted, using both weighed and RMS values could be a way to find the life range. From the results presented in figure 12 and table 2 the methodology to compute FCG life of bond strap reinforced plates can be considered validated for different substrate geometries, load levels, and strap materials and geometries. More validation cases can be found in [25].
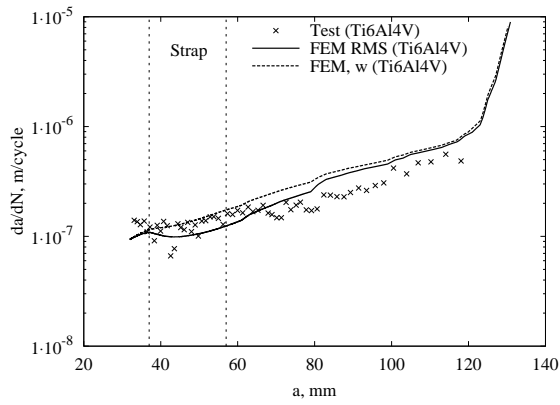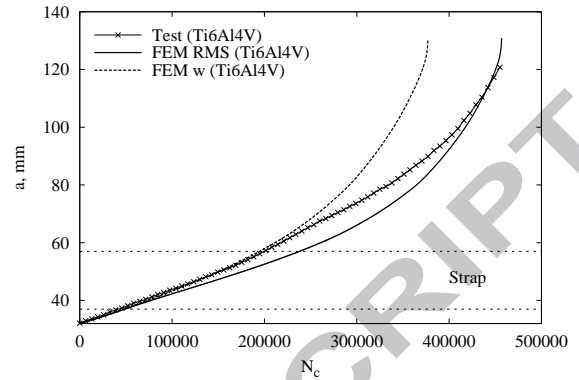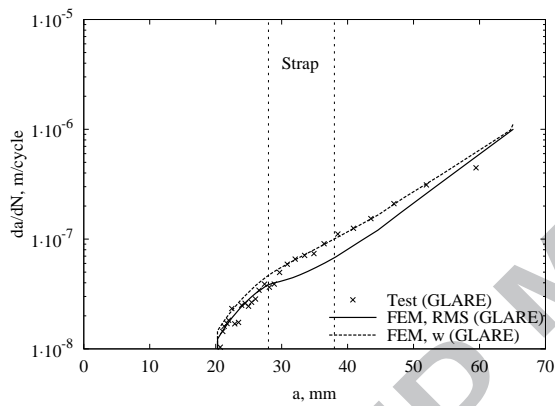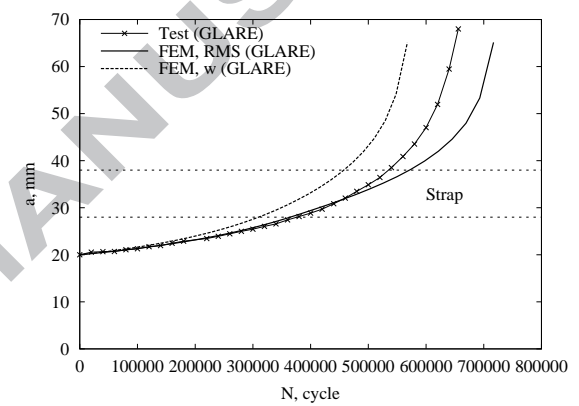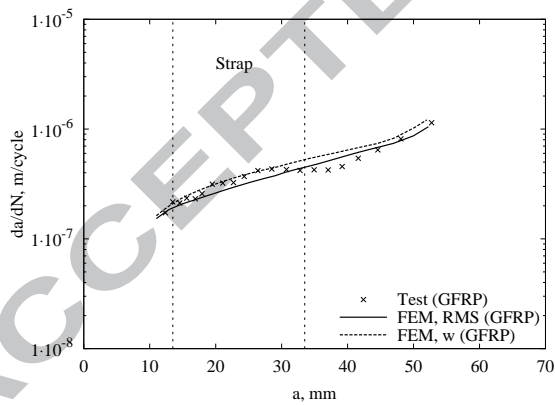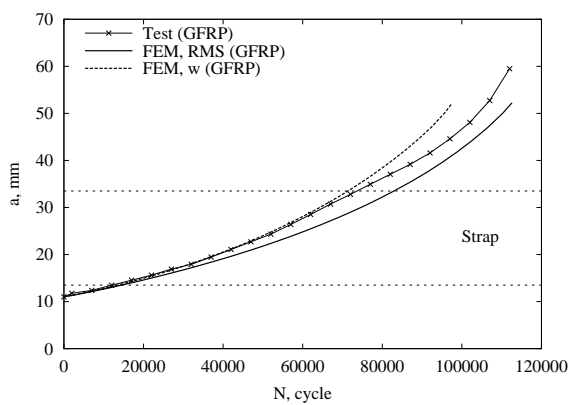
(a) FCG rate: SENT, Ti6Al4V strap $w20d5t2l200$

(b) FCG life: SENT, Ti6Al4V strap $w20d5t2l200$

(c) FCG rate, M(T), GLARE strap $w10d8t5.4l180$

(d) FCG life, M(T), GLARE strap $w10d8t5.4l180$

(e) FCG rate, M(T), GFRP strap $w20d2.5t4.4l180$

(f) FCG life, M(T), GFRP strap $w20d2.5t4.4l180$

Fig. 12. Validation of FCG rate and life against test results for SENT and M(T) samples reinforced by straps made of various materials; Experiments from [3,4,18].

17

Table 2
Predicted FCG lives and error ranges in comparison with test results (life in cycles)

	SENT + Titanium	M(T) + GLARE	M(T) + glass-epoxy
Test FCG life	455000 [3]	656000 [18]	112000 [4]
RMS	456900	717000	112600
(error)	(+0.42 %)	(+9.3 %)	(+0.5 %)
Weighted	377000	567400	94550
(error)	(- 17.1 %)	(-13.5 %)	(-15.5 %)

4. Conclusions

This paper has presented computational results and comparison with tests for validating the modelling methodology described in the first part of the two-part paper; validation cases are presented for each identified mechanism manifested in the bonded strap reinforced structures.

The SIF values calculated by the 2D FE model compares well with that obtained by a much more computational intensive 3D model.

Progressive adhesive failure is modelled by a quasi-static method using a mixed mode strain energy release rate criterion. Predicted final disbond shape and area agree with the experimental measurement.

Thermal residual stresses and their re-distribution with crack propagation are calculated for different strap materials and dimensions. Good agreement with the measured values is achieved for each strap configuration. Parameters influencing residual stresses are the elastic modulus and coefficient of thermal expansion of the adherends, strap size and the cure temperature.

Geometrical nonlinearity due to the secondary bending and its dependency on applied load and disbond area make it impossible to derive a non-dimensional SIF, i.e. the β factor. Therefore, SIF needs to be computed for each applied load level, and thermal and mechanical loads must be applied to the FE model simultaneously. For the cases presented in this paper, neglecting the thermal-mechanical coupling effect leads to an error of up to 20 %.

Finally, predicted fatigue crack growth rate and life are in reasonably good agreement with the tests.

One drawback of this modelling technique is the intensive computation caused by iterative calculations of the SIF due to substrate crack and disbond propagation. Excessive computing time will be needed when this methodology is applied to large-scale skin-stringer panels with multiple bonded straps. One possible solution is to develop and implement in the FE code an empirical law of disbond growth under fatigue loads.

18

References

[1] J. Schijve, Crack stoppers and arall laminates, Engineering Fracture Mechanics 37 (2) (1990) 405–421.

[2] M. B. Heinimann, R. J. Bucci, M. Kulak, M. Garratt, Improving damage tolerance of aircraft structures through the use of selective reinforcement, in: Proceedings 23rd Symposium of International Committee on Aeronautical Fatigue (ICAF), Hamburg, 2005, pp. 197–208.

[3] X. Zhang, D. Figueroa-Gordon, M. Boscolo, G. Allegri, P. E. Irving, Improving fail-safety of aircraft integral structures through the use of bonded crack retarders, in: Proceedings 24th Symposium of International Committee on Aeronautical Fatigue (ICAF), Naples, 2007.

[4] P. E. Irving, D. Figueroa-Gordon, X. Zhang, M. Boscolo, Bonded crack retarders for enhanced fail safety and damage tolerance in aircraft structures, in: Proceedings of 1st International Conference of Engineering Against Fracture (ICEAF), Patras, 2008.

[5] P. E. Irving, D. Figueroa-Gordon, Routes to improved damage tolerance; prediction of damage tolerant performance of high strength and hybrid structures, in: Proceedings of 1st International Conference on Damage Tolerance of Aircraft Structures (DTAS), Delft, 2007, http://www.dtas2007.nl accessed on September 2008.

[6] M. Boscolo, X. Zhang, A modelling technique for calculating stress intensity factors for structures reinforced by bonded straps. Part I: Mechanisms and formulation, Engineering Fracture Mechanics, Submited.

[7] M. Young, C. T. Sun, On the strain energy release rate for cracked plate subjected to out-of-plane bending moment, International Journal of Fracture 60 (1993) 227–247.

[8] C. Arendt, C. T. Sun, Bending effects of unsymmetric adhesively bonded composite repairs on cracked aluminum panels, in: Proceedings of the FAA/NASSA symposium on advanced integrity methods for airframe durability and damage tolerance, Pt. 1, Hampton, VA, 1994, pp. 33–48.

[9] C. T. Sun, J. Klung, C. Arendt, Analysis of cracked aluminium plates repaired with bonded composite patches, AIAA Journal 34 (2) (1996) 369–374.

[10] J. Klug, S. Maley, C. T. Sun, Characterization of fatigue behavior of bonded composite repairs, Journal of Aircraft 36 (6) (1999) 1016–1022.

[11] M. R. Lena, J. C. Klung, C. T. Sun, Composite patches as reinforcements and crack arresters in aircraft structures, Journal of Aircraft 35 (2) (1998) 318–324.

19

[12] R. Jones, R. J. Callinan, Finite element analysis of patched cracks, Journal Structural Mechanics 7 (1979) 107–130.

[13] H. Hosseini-Toudeshky, B. Mohammadi, A simple method to calculate the crack growth life of adhesively repaired aluminum panels, Composite Structures 79 (2007) 234–241.

[14] W.-Y. Lee, J.-J. Lee, Fatigue behavior of composite patch repaired aluminum plate, Journal of Composite Materials 39 (16) (2005) 1449–1463.

[15] S. Naboulsi, S. Mall, Modelling of a cracked metallic structure with bonded composite patch using the three layer technique, Composite Structures 35 (1996) 295–308.

[16] C. D. M. Liljedahl, M. E. Fitzpatrick, L. Edwards, Distortion and residual stresses in structures reinforced with titanium straps for improved damage tolerance, Materials Science and Engineering A 486 (2008) 104–111.

[17] C. D. M. Liljedahl, M. E. Fitzpatrick, L. Edwards, Residual stresses in structures reinforced with adhesively bonded straps designed to retard fatigue crack growth, Composite Structures 86 (2008) 344–355.

[18] D. Figueroa-Gordon, Bonded crack retarders internal reports and documentations, unpublished data, Cranfield University.

[19] J. Harter, AFGROW users guide and technical manual, Air Vehicles Directorate, afrl-va-wp-tr-2006-xxxx Edition (June 2006).

[20] M. Samprovalakis, Fatigue crack growth rate reduction in aircraft using bonded crack retarders, Master's thesis, Cranfield University, United Kingdom (2007).

[21] X. B. Lin, R. A. Smith, Finite element modelling of fatigue crack growth of surface cracked plates. Part I: The numerical technique, Engineering Fracture Mechanics 63 (1999) 503–522.

[22] C. D. M. Liljedahl, Bonded crack retarders internal reports and documentations, unpublished data, Open University.

[23] G. Glinka, Effect of residual stresses on fatigue crack growth in steel weldments under constant and variable amplitude load, Tech. Rep. STP 677, ASTM (1979).

[24] G. Servetti, X. Zhang, Predicting fatigue crack growth rate in a welded butt joint: The role of effective R ratio in accounting for residual stress effect, Engineering Fracture Mechanics 76 (11) (2009) 1589–1602.

[25] M. Boscolo, A finite element analysis of bonded crack retarders for integral aircraft structures, Ph.D. thesis, Cranfield University (2009).

20